Journal of Alloys and Compounds 657 (2016) 73–80

Contents lists available at ScienceDirect

Journal of Alloys and Compounds

journal homepage: http://www.elsevier.com/locate/jalcom

Nanostructured yttria dispersion-strengthened tungsten synthesized by sol–gel method

R. Liu [a], Z.M. Xie [a, b], Q.F. Fang [a, b, *], T. Zhang [a, **], X.P. Wang [a], T. Hao [a], C.S. Liu [a], Y. Dai [c]

[a] Key Laboratory of Materials Physics, Institute of Solid State Physics, Chinese Academy of Sciences, Hefei 230031, China
[b] University of Science and Technology of China, Hefei 230026, China
[c] Laboratory for Nuclear Materials, Paul Scherrer Institute, 5232 Villigen PSI, Switzerland

ARTICLE INFO

Article history:
Received 2 September 2015
Received in revised form
5 October 2015
Accepted 6 October 2015
Available online 14 October 2015

Keywords:
Tungsten
Microstructure
Sol–gel synthesis
Oxide dispersion strengthening

ABSTRACT

Yttria dispersion-strengthened tungsten with both enhanced strength and ductility was synthesized through sol–gel method followed by sintering and high-temperature swaging. The sol–gel synthesis process involving a molecular-level doping leads to a unique nanostructure that Y_2O_3 nano-particles were homogeneously dispersed in tungsten grains interior. The nanosized Y_2O_3 particles in sol–gel synthesized W-1%Y_2O_3 are stable in size even under a high sintering temperature of 2300 °C. The swaged sol–gel W-1%Y_2O_3 show ductility at a relative low temperature of 250 °C, which is about 100 °C and 250 °C lower than that of spark-plasma-sintered sol–gel W-1%Y_2O_3 and ball-milling synthesized W-1% Y_2O_3, respectively. The sol–gel method provides a promising access to high-performance nanostructured tungsten materials with both high strength and ductility, and can be easily scaled for industrial production.

1. Introduction

Owing to the excellent properties such as high melting temperature (3422 °C), low coefficient of thermal expansion, low vapor pressure and high tensile strength, tungsten has been used for high-temperature and electric applications. Besides, tungsten has also been considered as one of the most promising candidates for plasma facing materials in fusion reactors due to its high sputtering resistance, high thermal conductivity and low tritium retention properties [1–5]. However, tungsten exhibits serious embrittlement in several aspects, i.e., low-temperature brittleness (relative high ductile-to-brittle transition temperature (DBTT) > 400 °C), recrystallization brittleness and irradiation induced brittleness [5–7]. These disadvantages make it difficult to shape tungsten and limit the applications of tungsten materials especially in safety-critical applications. Therefore, tungsten alloys with excellent mechanical properties and high-temperature stability are highly desirable.

It is generally understood that a major cause of the low toughness of W alloys is their sensitivity to some impurities such as O and N, which could segregate on the grain boundaries (GBs) and decrease the GBs cohesion [6–9]. Therefore, methods that modify impurities distributions and strengthen GBs would be effective in improving the strength and toughness. Reducing impurities via vacuum and zone melting may lower the DBTT to about 200 °C [10]. However, pure W has low high-temperature strength and undergoes recrystallization at relatively low temperature (~1200 °C) which further reduces the fracture toughness [11]. Adding rhenium could reduce the DBTT and increase the recrystallization temperature [12], but this would increase the cost because of the expensive rhenium. Besides, neutron irradiated W–Re alloys also showed drastic radiation-induced embrittlement and hardening by precipitation [13].

Refining the grains to obtain ultrafine-grained or nano-grained W through severe plastic deformation could increase GBs area and decrease the average concentration of impurities at GBs, and thus improve the strength and the toughness of W [7–10]. Besides, the large amount of grain boundaries or phase interfaces in nanostructured materials may act as sinks for irradiation induced point defects, which would improve the irradiation resistance of materials [11,14,15]. Nevertheless, the large volume fraction of GBs also leads to an inherent instability especially under high temperature

* Corresponding author. Key Laboratory of Materials Physics, Institute of Solid State Physics, Chinese Academy of Sciences, Hefei 230031, China.
** Corresponding author.
E-mail addresses: liurui@issp.ac.cn (R. Liu), qffang@issp.ac.cn (Q.F. Fang), zhangtao@issp.ac.cn (T. Zhang).

http://dx.doi.org/10.1016/j.jallcom.2015.10.059
0925-8388/

[16]. During the high temperature sintering or usage process, the mechanical properties and irradiation resistance of nano-grained tungsten would be degraded with the grain coarsening. Therefore, the high temperature stability of nano-grained tungsten materials must be improved. Dispersing small amounts of thermally stable oxide particles, such as La_2O_3 and Y_2O_3 into W and forming the so-called oxide-dispersion-strengthened W (ODS-W), can refine the grains and inhibit the movement of dislocations and GBs, and thus increase the high-temperature strength, recrystallization temperature and creep resistance [17–22]. However, the increase of strength is often accompanied with the decrease of ductility in traditionally produced ODS-W. One major reason is that, the oxide particles in traditional ODS-W are large in size and usually distributed at GBs [14,23,24], which would act as stress concentrators and weaken the cohesion of GBs, leading to intergranular fracture and low toughness. Therefore, to improve the mechanical properties of tungsten, the microstructures including the size and distribution of oxide particles should be designed to reduce the stress concentration caused by coarse oxide particles at GBs.

In this work, sol–gel method providing molecular-level mixing was used for the synthesis of nanostructured yttria (Y_2O_3) dispersion-strengthened tungsten materials, in which Y_2O_3 particles are nanoscale and most of them were homogeneously dispersed in tungsten grains interior. Large sol–gel W-1%Y_2O_3 rods with excellent mechanical properties were obtained through conventional sintering followed by hot rotary swaging. The Y_2O_3 nanoparticles in tungsten grains interior could improve the strength by pinning dislocations and alleviate the stress-concentration caused by the segregation of coarse particles at GBs, and thus lead to enhanced strength and ductility.

2. Experimental

2.1. Synthesis and processing of materials

Oxide dispersed tungsten powders with a nominal composition of W-1wt%Y_2O_3 were synthesized by sol–gel method [24]. Citric acid ($C_6H_8O_7\cdot H_2O$) and yttrium nitrate hydrate $Y(NO_3)_3\cdot 6H_2O$ were firstly dissolved in deionized water, and then ammonium paratungstate $(NH_4)_{10}[H_2W_{12}O_{42}]\cdot 4H_2O$ was added into the solution. Citric acid is employed as chelating agent, which provides the mixing of cations at the molecular level in sol–gel process. The solution was heated at 80 °C with continuous stirring to remove excess water. The resulting gel was dried at 120 °C and then was calcined at 550 °C in air to remove the organic compounds, leading to a light-yellow mixture of tungsten oxides and yttrium oxides. Then the oxides mixture was reduced in flowing hydrogen, resulting in Y_2O_3 doped tungsten powders. Both submicron and micron tungsten powders were prepared at different hydrogen-reduction temperatures, 800 °C and 850 °C, respectively. The C, N, O contents in the sol–gel synthesized W-1%Y_2O_3 powders are 0.068 wt%, 0.034 wt% and 0.270 wt%, respectively. It is worth pointing out that the total oxygen content of 0.270 wt% includes 0.213 wt% oxygen from Y_2O_3.

Small tungsten samples from sol–gel synthesized sub-micron powders were consolidated using spark plasma sintering (SPS) method [25]. The as-prepared powders were loaded into a graphite mold at first and then under a uniaxial pressure of 50.9 MPa, heated to 1800 °C by a pulse current (1000–5000 A) and hold for 2 min. The heating rate at temperatures below and above 1300 °C was 100 °C/min and 50 °C/min, respectively. The cooling rate was 100 °C/min. The size of the sintered samples was 20 mm in diameter and about 2.0 mm in thickness. As a comparison, W-1wt%Y_2O_3 samples from ball-milling produced powders were also fabricated by SPS. For this purpose, commercial tungsten powders (average particle size 600 nm, purity 99.9%) and nano-size Y_2O_3 particles (50 nm, purity 99.99%) were used as starting materials. The powders were ball-milled in a planetary ball mill for 4 h in argon atmosphere with a rotation speed of 240 rpm. The ball-to-powder weight ratio was 8:1. Tungsten carbide balls and mortars were used to minimize the possible impurity contamination. The chemical content of the commercial tungsten powders was list in Table 1. Both the sol–gel synthesized and ball-milling produced tungsten powders were consolidated following the same SPS procedures.

Large sol–gel W-1%Y_2O_3 rods were fabricated by using micron-sized tungsten powders synthesized by sol–gel method. The sol–gel synthesized micron-sized tungsten powders were compacted into a cylindrical rod with a diameter of 16 mm by cold isostatic pressing and then sintered at 2300 °C for 4 h in flowing dry hydrogen. The diameter of the sintered tungsten rod was about 14 mm. Then the sintered tungsten was heated at 1600 °C in hydrogen atmosphere and was swaged into a rod with a diameter of 9.1 mm and a length of about 800 mm. The consolidation and hot swaging were carried out by collaborating with Beijing Tianlong Tungsten & Molybdenum Co., Ltd.

2.2. Mechanical tests

The tensile experiments of tungsten materials were conducted at various temperatures from room-temperature to 600 °C by using an Instron-5967 machine. The tensile speed is 0.06 mm/min. Before tensile testing, tungsten samples were cut by electric discharge machining (EDM) and polished into dog-bone-shaped samples with a cross-section of 1.5 × 0.75 mm^2 and a working length of 5 mm [26]. For spark-plasma-sintered (SPSed) tungsten alloys, tensile-testing specimens were cut along radial direction. While for the swaged tungsten samples, the tensile loading direction was parallel to the elongation direction of swaging. The hardness of tungsten was measured at room-temperature using Vickers microhardness testing with a load of 200 g and a dwell time of 15 s.

2.3. Microstructure characterization

The morphology of the synthesized powders and the fracture surfaces of tensile-tested samples were characterized with a field-emission scanning electron microscopy (FESEM, Sirion 200, FEI). Tungsten samples were polished and etched for metallographic characterization. The microstructures of the synthesized powders and sintered tungsten bulks were investigated using a JEOL JEM-2000FX transmission electron microscope (TEM).

3. Results and discussion

3.1. Microstructure of synthesized powders

The SEM micrographs of sol–gel synthesized W-1%Y_2O_3 powders and ball-milling produced W-1%Y_2O_3 powders were shown in Fig. 1. The average particle size of ball-milling produced W-1%Y_2O_3 powders is about 600 nm (Fig. 1a). Fig. 1b and c show the sol–gel synthesized W-1%Y_2O_3 powders reduced at 800 °C and 850 °C, respectively. The size of tungsten particles in sol–gel W-1%Y_2O_3 powders reduced at 800 °C is about 100–400 nm (Fig. 1b), while

Table 1
Chemical compositions of the as-received tungsten powders (wt.%).

	O	C	P	S	N	Fe	Cr	Ti	W
W powder	0.24	0.0029	0.0005	0.0005	–	0.001	0.0005	0.0005	Bal

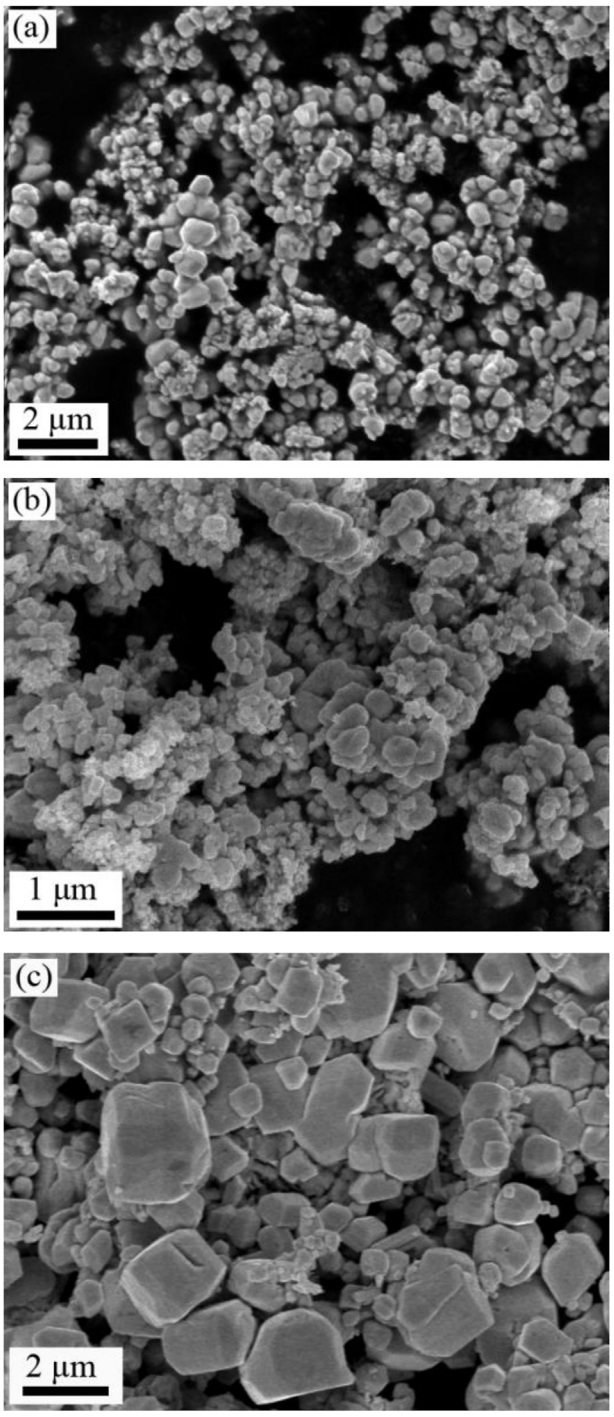

Fig. 1. SEM images of ball-milling produced tungsten powders (a) and sol–gel synthesized W-1%Y_2O_3 powders hydrogen-reduced at 800 °C (b) and 850 °C (c).

that of sol–gel W-1%Y_2O_3 powders reduced at 850 °C is 0.2–3.0 μm (Fig. 1c). Sol–gel W-1%Y_2O_3 powders with larger tungsten particles sizes were prepared due to their better flow properties, which are easier for industrial production.

Fig. 2a and 2b shows the TEM images of sol–gel W-1%Y_2O_3 powders hydrogen-reduced at 800 °C and 850 °C, respectively. In both batches of sol–gel W-1%Y_2O_3 powders, nano-size Y_2O_3 particles (indicated by arrows) can be found in tungsten particles interior, although the size of tungsten particles is different. As these Y_2O_3 nano-particles are isolated by tungsten matrix and have low

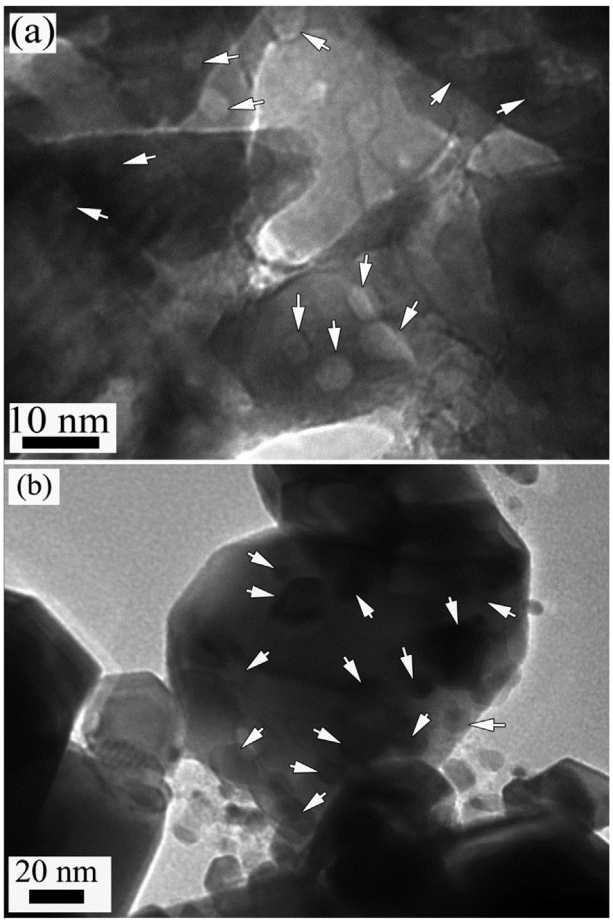

Fig. 2. TEM images of sol–gel synthesized W-1%Y_2O_3 powders hydrogen-reduced at 800 °C (a) and 850 °C (b).

chance to combine with other Y_2O_3 particles, they would be more likely to stay in tungsten grains interior and keep small size even during high-temperature sintering process. Therefore, the number and size of Y_2O_3 particles on tungsten GBs could be reduced effectively, and thus the stress-concentration can be alleviated.

3.2. Microstructure and mechanical properties of spark-plasma-sintered W-1%Y_2O_3 from sol–gel and ball-milling synthesized powders

The relative density, grain size and Vickers micro-hardness of SPSed W-1%Y_2O_3 samples were listed in Table 2. The relative density of SPSed sol–gel W-1%Y_2O_3 and ball-milling W-1%Y_2O_3 is 99.5% and 99.0%, respectively. Fig. 3 shows the engineering stress-strain curves of spark-plasma-sintered ball-milling W-1%Y_2O_3 and sol–gel W-1%Y_2O_3. The ultimate tensile strength (UTS) and total elongation (TE) of W-1%Y_2O_3 were listed in Table 3. The sol–gel W-1%Y_2O_3 showed significant improvement in both strength and ductility as compared to the ball-milling W-1%Y_2O_3. The UTS of sol–gel W-1%Y_2O_3 at 400 °C is 572 MPa and the TE is 11.2%, while the UTS of ball-milling W-1%Y_2O_3 is only 472 MPa and the engineering stress-strain showed typical brittle fracture (Fig. 3a). The UTS and TE of sol–gel W-1%Y_2O_3 at 350 °C is 632 MPa and 1.6%, respectively. At 500 °C the UTS of sol–gel W-1%Y_2O_3 is 522 MPa, which is comparable with that of ball-milling W-1%Y_2O_3 (538 MPa), but the TE (16.8%) is about four times higher than that of the ball-milling W-1%Y_2O_3 (3.6%). At 600 °C, the UTS and TE of SPSed

Table 2
Density, grain size and Vickers micro-hardness of the W-1%Y_2O_3 alloys.

Materials	Density (g/cm^3)	Relative Density (%)	Grain size (μm)	H_{V100g} (GPa)
SPSed ball-milling W-1%Y_2O_3	18.581	99.0 ± 0.2	3.2	5.21 ± 0.1
SPSed sol–gel W-1%Y_2O_3	18.667	99.5 ± 0.1	3.9	4.63 ± 0.1
Swaged sol–gel W-1%Y_2O_3	18.562	98.9 ± 0.1	226[a]/54[b]	4.61 ± 0.1

[a] Average tungsten grain size parallel to swaging direction.
[b] Average tungsten grain size perpendicular to swaging direction.

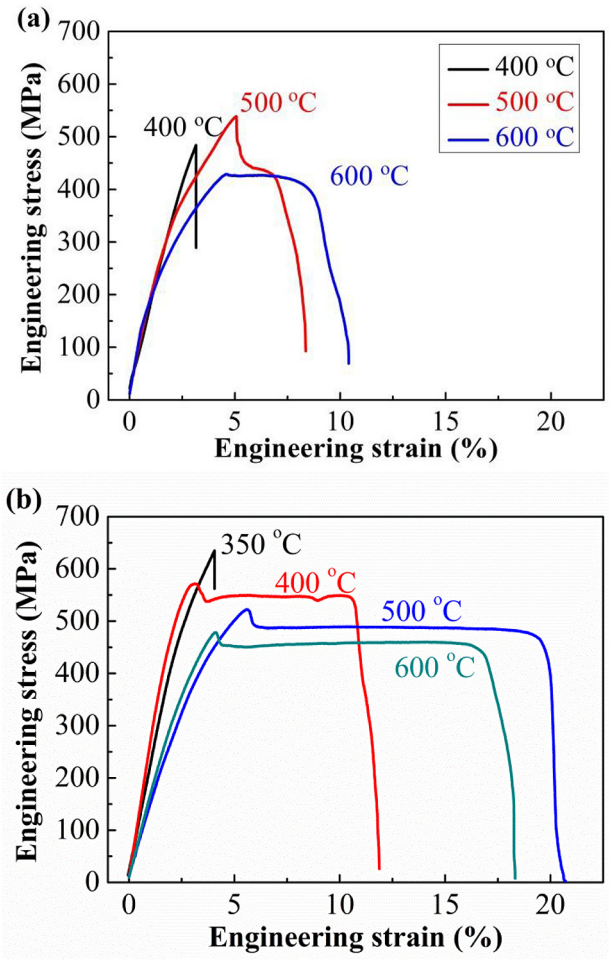

Fig. 3. Tensile stress-strain curves of (a) SPSed ball-milling W-1%Y_2O_3 and (b) SPSed sol–gel W-1%Y_2O_3 at various temperatures.

sol–gel W-1%Y_2O_3 are 478 MPa and 15.2%, respectively. Both the UTS and TE of sol–gel W-1%Y_2O_3 are higher than those of ball-milling W-1%Y_2O_3 (430 MPa and 8.8%). Besides, the SPSed sol–gel W-1%Y_2O_3 also showed ductility at lower temperatures, implying lower DBTT than the SPSed ball-milling W-1%Y_2O_3. These results suggest that the sol–gel synthesis process is a promising method to fabricate ODS-W with both high strength and extraordinary ductility.

It is well known that the mechanical properties are highly determined by the microstructure of materials. To investigate the mechanism of enhanced mechanical properties in sol–gel synthesized ODS-W alloys, the microstructure of both SPSed ball-milling W-1%Y_2O_3 and SPSed sol–gel W-1%Y_2O_3 was characterized by TEM (Fig. 4). It can be seen that the distribution and size of Y_2O_3 particles are significantly different for the two alloys. In SPSed sol–gel W-1%Y_2O_3, as shown in Fig. 4b–c, most of the Y_2O_3 particles were homogeneously dispersed in tungsten grains interior, and very few Y_2O_3 particles were found on tungsten GBs. Most Y_2O_3 particles are near spherical and the average particle size is about 30 nm. The intragrannular Y_2O_3 nano-particles could generate and pin dislocations, and enhance the strength and ductility of tungsten without initiating cracks at GBs. By reducing the number and size of Y_2O_3 particles at GBs through sol–gel process, the stress-concentration and brittleness induced by large oxide particles segregation at GBs can also be effectively alleviated in sol–gel W-1%Y_2O_3. Therefore, the excellent mechanical properties of sol–gel W-1%Y_2O_3 originate from the unique microstructures obtained through the sol–gel synthesis process.

In ball-milling W-1%Y_2O_3 however, many coarse yttrium oxide particles larger than 400 nm were found at GBs (see Fig. 4a), and only small amount of nano-sized Y_2O_3 particles were found in tungsten grains interior. The oxide particles at GBs are larger in size and elongated along grain boundaries, as indicated by arrows in Fig. 4a. These Y_2O_3 particles at GBs may hinder GBs migration and inhibit grain growth, and thus improve the strength and high-temperature stability of tungsten [19]. However, large Y_2O_3 particles at GBs would also induce stress/strain concentration and tend to localize strains, which may become the starting points of possible cracks and reduce the toughness of material [23]. Severe stress concentration induced at the coarse particles would cause interfacial decohesion at weaker GBs or particle cracking, and thus result in microcracks along GBs and intergranular fracture. These would definitely reduce the ductility of tungsten. Besides, as most Y_2O_3 particles segregate at GBs and form large particles, the number density of Y_2O_3 particles in tungsten grains would be reduced and the dispersion-strengthening effect of oxide particles was inhibited.

The differences in microstructures including size and distribution of Y_2O_3 particles in W-1%Y_2O_3 alloys can be derived from the microstructure of initial powders. For sol–gel synthesized

Table 3
Tensile properties of W-1%Y_2O_3 alloys.

Materials	Tensile strength (MPa)/elongation (%)					
	200 °C	250 °C	300 °C	400 °C	500 °C	600 °C
SPSed ball-milling W-1%Y_2O_3	–	–	–	472/-	538/3.6	430/8.8
SPSed sol–gel W-1%Y_2O_3	–	–	632/1.6[a]	572/11.2	522/16.8	478/15.2
Swaged sol–gel W-1%Y_2O_3	619/1.6	544/3.8	506/13.6	497/14.8	503/15.6	478/14.2

[a] Measured at 350 °C.

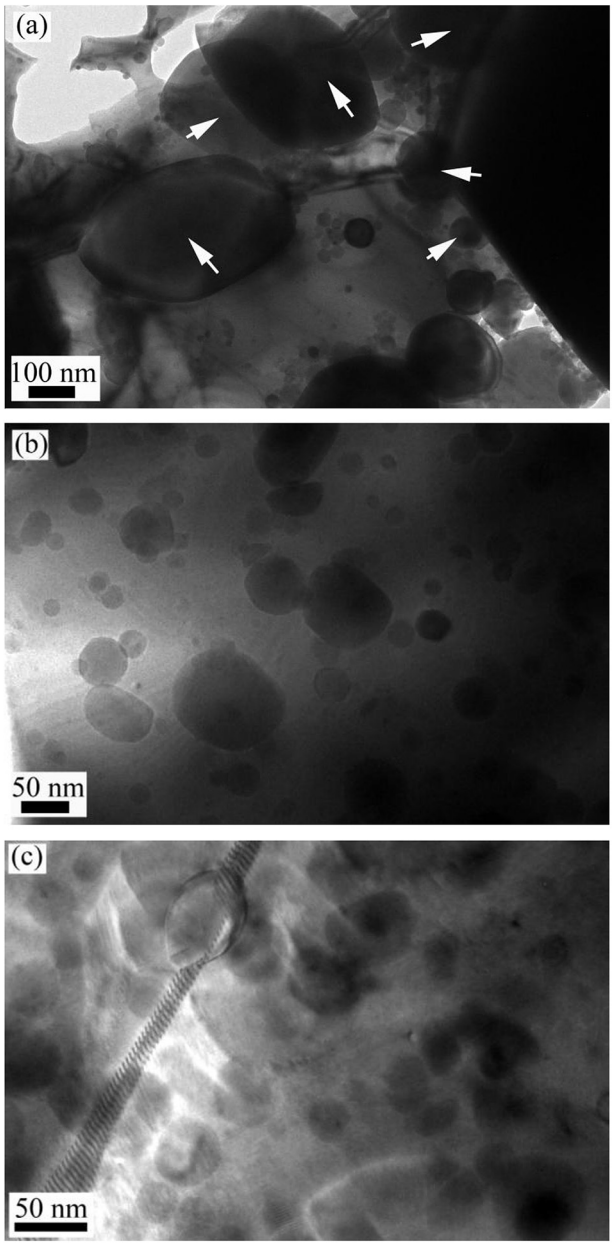

Fig. 4. TEM images of (a) ball-milling W-1%Y_2O_3 and (b–c) sol–gel W-1%Y_2O_3 produced by spark-plasma-sintering.

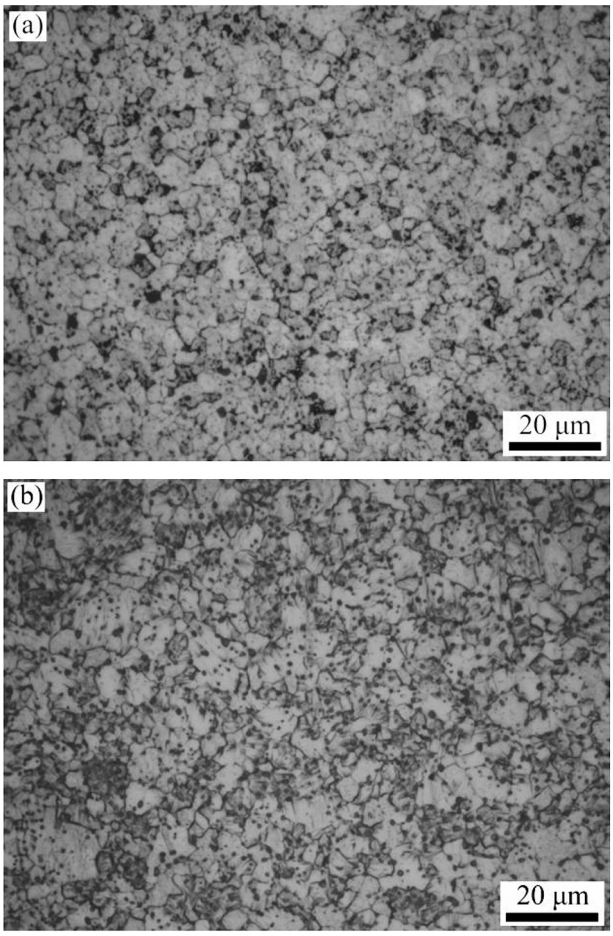

Fig. 5. Optical micrographs of (a) ball-milling W-1%Y_2O_3 and (b) sol–gel W-1%Y_2O_3 produced by spark-plasma-sintering.

powders, as many Y_2O_3 nano-particles were isolated in tungsten particles, they have less chance to aggregate with other Y_2O_3 particles. Therefore, these particles are small in size and stay in tungsten grains even sintered at high temperature. In ball-milling produced powders, Y_2O_3 and tungsten particles were mixed together, but Y_2O_3 particles were not embedded in tungsten particles. When tungsten particles grow into larger grains during the high-temperature sintering process, the initial nano-sized Y_2O_3 particles between tungsten particles tend to aggregate to grow into larger Y_2O_3 particles at GBs (See Fig. 4a). As a result, the ductility of ball-milling W-1%Y_2O_3 was reduced due to the segregation of larger particles at GBs.

The grain size and hardness of the two alloys were also affected by the microstructure of initial powders. Fig. 5 shows the optical images of SPSed ball-milling W-1%Y_2O_3 and sol–gel W-1%Y_2O_3. The average grain size of SPSed ball-milling W-1%Y_2O_3 and sol–gel W-1%Y_2O_3 is 3.2 μm and 3.9 μm, respectively. The finer grain size in the SPSed ball-milling W-1%Y_2O_3 is reasonable, because many Y_2O_3 particles at GBs (see Fig. 4a) could inhibit the migration of GBs and lead to smaller tungsten grain size. The Vickers micro-hardness of SPSed sol–gel W-1%Y_2O_3 and ball-milling W-1%Y_2O_3 is 4.63 GPa and 5.21 GPa, respectively. The higher hardness of SPSed ball-milling W-1%Y_2O_3 may also due to its finer grain size according to Hall–Petch relation.

The fracture surfaces of SPSed ball-milling W-1%Y_2O_3 and sol–gel W-1%Y_2O_3 tensile-tested at different temperatures were observed with SEM, as shown in Fig. 6. Fig. 6a showed the micrograph of sol–gel W-1%Y_2O_3 tensile-tested at 300 °C. Both transgranular and intergranular fractures were found in the fracture surface of sol–gel W-1%Y_2O_3, but the fraction of intergranular fractures is lower than that of ball-milling W-1%Y_2O_3 tensile-tested at 400 °C (Fig. 6c). In Fig. 6b, deformed tungsten grains in sol–gel W-1%Y_2O_3 tensile-tested at 400 °C suggest that SPSed sol–gel W-1%Y_2O_3 is ductile at 400 °C, which is consistent with the tensile-test results (Fig. 3b). While in the ball-milling W-1%Y_2O_3 tested at 400 °C and even at a higher temperature of 500 °C, intergranular fractures were dominant in the tensile fractured surfaces, as shown in Fig. 6c–d. These results imply that cracks initiate more likely along the GBs and the cohesion strength of GBs is much lower than the strength of grains in the SPSed ball-milling W-1%Y_2O_3. In sol–gel W-1%Y_2O_3, the higher fraction of transgranular fracture suggests improved cohesion strength of GBs, which could be attributed to the small size and reduced number of Y_2O_3 particles at GBs.

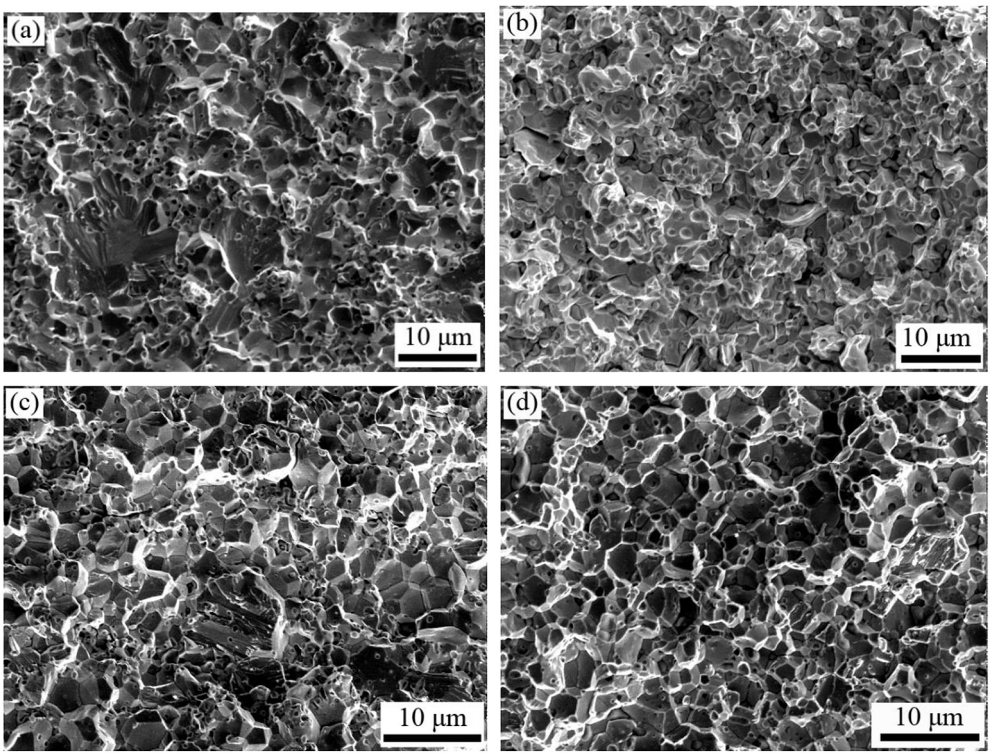

Fig. 6. SEM fractographs of the SPSed sol–gel W-1%Y_2O_3 tensile-tested at 300 °C (a) and 400 °C (b), and the SPSed ball-milling W-1%Y_2O_3 tensile-tested at 400 °C (c) and 500 °C (d).

3.3. *Mechanical property and microstructure of swaged sol–gel W-1%Y_2O_3*

As the sol–gel W-1%Y_2O_3 showed excellent mechanical properties including both high strength and ductility, larger samples were produced through industrial processes involving high-temperature sintering and hot swaging. The swaged sol–gel W-1%Y_2O_3 samples are rods with a diameter of 9.1 mm and a length of about 800 mm. Fig. 7 shows the engineering strain-stress curves of the swaged sol–gel W-1%Y_2O_3 at temperatures from 200 °C to 600 °C. The UTS and TE of the swaged sol–gel W-1%Y_2O_3 at 200 °C is 619 MPa and 1.6%, respectively. At 250 °C, the swaged sol–gel W-1%Y_2O_3 showed obvious tensile plastic deformation with a TE of 3.8% and UTS of 544 MPa. With the testing temperatures increasing from 300 °C to 500 °C, the TE increases from 13.6% to 15.6%, while the UTS is relatively stable and remains about 500 MPa.

At temperatures below 500 °C, the tensile strength of the swaged sol–gel W-1%Y_2O_3 is lower than that of the SPSed sol–gel W-1%Y_2O_3. This could be attributed to the larger grain size of the swaged sol–gel W-1%Y_2O_3. Nevertheless, the swaged sol–gel W-1% Y_2O_3 showed comparable strength at higher temperatures. Although the enhancement of strength by hot swaging is not obvious due to the large grain size, the low temperature ductility can be improved effectively as compared to the SPSed W-1%Y_2O_3 alloys. Fig. 8 shows the tensile elongation of all the W-1%Y_2O_3 alloys

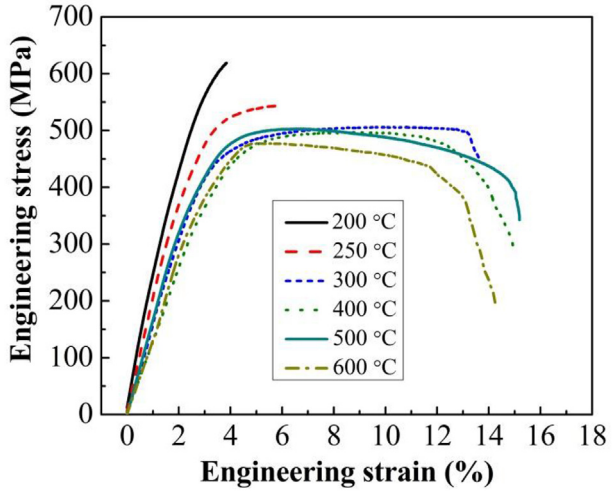

Fig. 7. Tensile stress-strain curves of the swaged sol–gel W-1%Y_2O_3 at various temperatures.

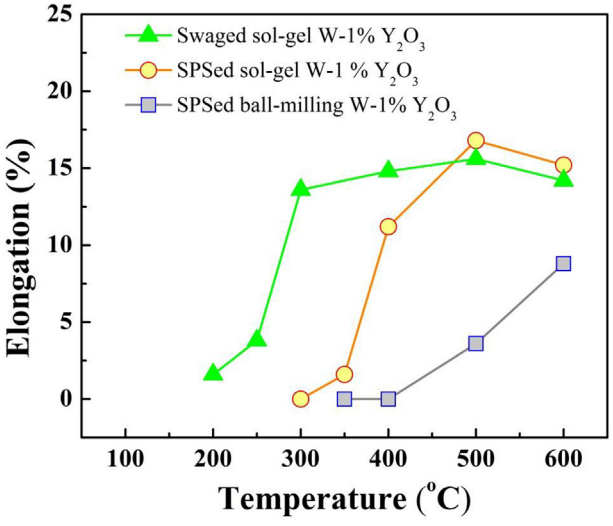

Fig. 8. Total elongation of different W-1%Y_2O_3 alloys tensile-tested at various temperatures.

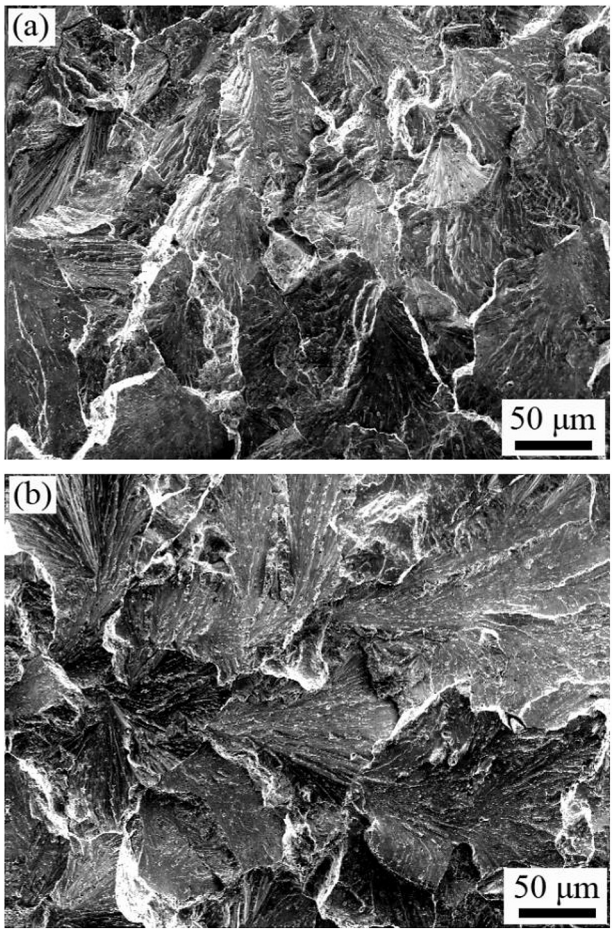

Fig. 9. SEM images of the fracture surfaces of the swaged sol–gel W-1%Y_2O_3 tensile-tested at room-temperature (a) and 250 °C (b).

at various temperatures. It can be seen that the swaged sol–gel W-1%Y_2O_3 showed obvious ductility at about 250 °C, which is about 100 °C and 250 °C lower than those of the SPSed sol–gel W-1%Y_2O_3 and ball-milling W-1%Y_2O_3, respectively. This result indicates that the low-temperature ductility of ODS-W can be effectively improved by hot swaging.

Fig. 9 shows the typical fracture surfaces of the swaged sol–gel W-1%Y_2O_3 tensile-tested at room-temperature and 250 °C, respectively. Transgranular fracture is the dominant type of failure in the swaged sol–gel W-1%Y_2O_3 tensile-tested at room-temperature (see Fig. 9a) and 250 °C (Fig. 9b), while the SPSed W-1%Y_2O_3 alloys showed many intergranular fractures (see Fig. 6), even though they were tensile-tested at higher temperatures. These results suggest that the cohesion strength of GBs has been effectively enhanced by hot swaging process. The reason may be that tungsten grains were pressed and shaped during the hot swaging processes, which leads to elongated tungsten grains parallel to flow direction and strengthened cohesion of GBs.

Fig. 10 shows the TEM and high-resolution transmission electron microscopy (HRTEM) images of the swaged sol–gel W-1%Y_2O_3. Most nano-sized Y_2O_3 particles were homogeneously dispersed in tungsten grains interior, as shown in Fig. 10a–c. In Fig. 10a, it can be seen that some Y_2O_3 particles are at GBs, but they are much smaller than those in SPSed ball-milling W-1%Y_2O_3. Fig. 10d shows the typical HRTEM lattice image of Y_2O_3 particle in tungsten grains interior. Dispersing nanosized particles in grain interior is an effective method to improve the strength and the ductility, because the intragranular particles can generate, pin down and thus accumulate dislocations within the grains [23]. Similar approach was successfully used in ODS Mo alloys and age-hardening Al alloys [23,27]. Therefore, the unique microstructure that nanosized Y_2O_3 particles were homogeneously dispersed in tungsten grains interior could be the main reason of the enhanced mechanical properties in the swaged sol–gel W-1%Y_2O_3.

Fig. 11 shows the size distribution of Y_2O_3 particles in the swaged sol–gel W-1%Y_2O_3. The average size of Y_2O_3 particles in tungsten grain interior is only 52 nm, even though the sol–gel W-

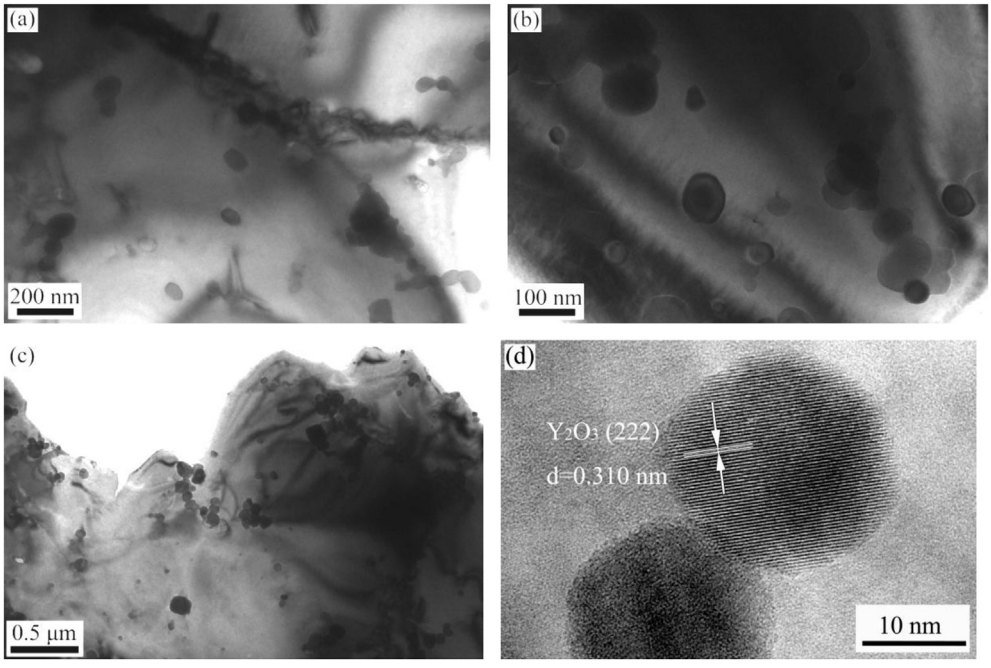

Fig. 10. TEM images of the swaged sol–gel W-1%Y_2O_3 observed in different areas (a–c), and HRTEM image of Y_2O_3 particles in tungsten grains interior (d).

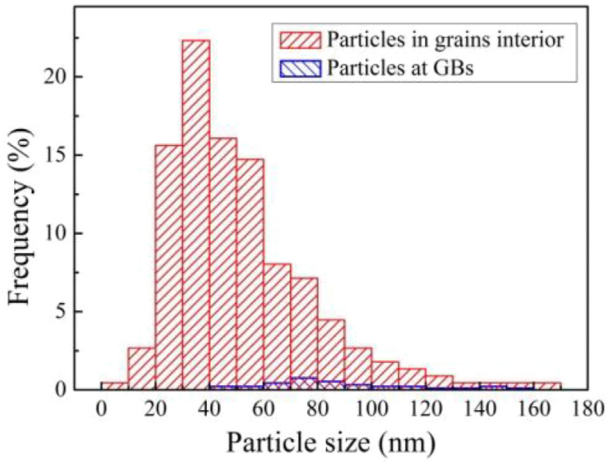

Fig. 11. Size distribution of Y_2O_3 particles in the swaged sol–gel W-1%Y_2O_3.

1%Y_2O_3 rods were sintered at temperature as high as 2300 °C for several hours. The Y_2O_3 particles at GBs are also small in size with an average size of about 84 nm. Besides, the very low frequency of Y_2O_3 particles at GBs indicates that Y_2O_3 particles were mainly distributed in tungsten grains interior. The fine particle size of Y_2O_3 could be attributed to that many Y_2O_3 nano-particles were isolated in tungsten particles interior by sol–gel synthesis process, because these isolated Y_2O_3 particles have little chance to aggregate with other Y_2O_3 particles. Therefore, the Y_2O_3 particles were small in size and homogeneously dispersed in tungsten grains interior even under a very high sintering temperature of 2300 °C. This further shows the advantage of sol–gel method in the fabrication of nanostructured W-Y_2O_3 alloys with excellent high-temperature stability.

4. Conclusions

Nanostructured W-1%Y_2O_3 with Y_2O_3 nano-particles homogeneously dispersed in tungsten grains interior were synthesized by sol–gel method. Spark-plasma-sintered sol–gel W-1%Y_2O_3 showed significant enhancement in tensile strength, elongation, and low-temperature ductility as compared with the SPSed ball-milling W-1%Y_2O_3. The oxide particles in the SPSed sol–gel W-1%Y_2O_3 are nearly spherical with an average particle size of about 30 nm and most of them were homogeneously dispersed in tungsten grains interior. The nano-particles in tungsten grains interior could generate and store dislocations without causing cracks localized at GBs, and thus improve the strength and ductility of tungsten materials. While in ball-milling W-1%Y_2O_3, Y_2O_3 particles tend to aggregate and form coarser particles at GBs, which tend to induce stress/strain concentration and cause microcracks along the GBs. Large sol–gel W-1%Y_2O_3 rods fabricated through industrial sintering method and hot-swaging also showed improved mechanical properties especially the low-temperature ductility. The size of Y_2O_3 particles is nano-scale with an average particle size of 52 nm and most Y_2O_3 particles were homogeneously dispersed in tungsten grains interior even under a high sintering temperature of 2300 °C. This shows the excellent high-temperatures stability of Y_2O_3 nanoparticles in sol–gel synthesized ODS-W materials. In general, the sol–gel method in this work provides a promising access to high-performance nanostructured tungsten with both high strength and ductility, and this method can be easily used for industrial production.

Acknowledgments

This work was supported by the National Magnetic Confinement Fusion Program (Grant No. 2015GB112000), and the National Natural Science Foundation of China (Grant Nos. 51301164, 11274305, 11475216), and the Anhui Provincial National Natural Science Foundation of China (1408085QE77).

References

[1] I. Smid, H.D. Pacher, G. Vieider, U. Mszanowski, Y. Igitkhanov, G. Janeschitz, J. Schlosser, L. Plochl, J. Nucl. Mater. 233–237 (1996) 701–707.
[2] T. Hino, M. Akiba, Fusion Eng. Des. 49–50 (2000) 97–105.
[3] P. Norajitra, L.V. Boccaccini, E. Diegele, V. Filatov, A. Gervash, R. Giniyatulin, S. Gordeev, V. Heinzel, G. Janeschitz, J. Konys, W. Krauss, R. Kruessmann, S. Malang, I. Mazul, A. Moeslang, C. Petersen, G. Reimann, M. Rieth, G. Rizzi, M. Rumyantsev, R. Ruprecht, V. Slobodtchouk, J. Nucl. Mater. 329–333 (2004) 1594–1598.
[4] E. Diegele, R. Krussmann, S. Malang, P. Norajitra, G. Rizzi, Fusion Eng. Des. 66–68 (2003) 383–387.
[5] P. Norajitra, L.V. Boccaccini, A. Gervash, R. Giniyatulin, N. Holstein, T. Ihli, G. Janeschitz, W. Krauss, R. Kruessmann, V. Kuznetsov, A. Makhankov, I. Mazul, A. Moeslang, I. Ovchinnikov, M. Rieth, B. Zeep, J. Nucl. Mater. 367–370 (2007) 1416–1421.
[6] H. Kurishita, S. Kobayashi, K. Nakai, T. Ogawa, A. Hasegawa, K. Abe, H. Arakawa, S. Matsuo, T. Takida, K. Takebe, M. Kawai, N. Yoshida, J. Nucl. Mater. 377 (2008) 34–40.
[7] H. Kurishita, Y. Amano, S. Kobayashi, K. Nakai, H. Arakawa, Y. Hiraoka, T. Takida, K. Takebe, H. Matsui, J. Nucl. Mater. 367–370 (2007) 1453.
[8] Y. Zhang, A.V. Ganeev, J.T. Wang, J.Q. Liu, I.V. Alexandrov, Mater. Sci. Eng. A 503 (2009) 37–40.
[9] Y. Ishijima, H. Kurishita, K. Yubuta, H. Arakawa, M. Hasegawa, Y. Hiraoka, T. Takida, K. Takebe, J. Nucl. Mater. 329–333 (2004) 775–779.
[10] L.J. Kecskes, K.C. Cho, R.J. Dowding, B.E. Schuster, R.Z. Valiev, Q. Wei, Mater. Sci. Eng. A Struct. 467 (2007) 33–43.
[11] H. Kurishita, T. Kuwabara, M. Hasegawa, S. Kobayashi, K. Nakai, J. Nucl. Mater. 343 (2005) 318–324.
[12] W. Setyawan, R.J. Kurtz, Scr. Mater. 66 (2012) 558–561.
[13] Y. Nemoto, A. Hasegawa, M. Satou, K. Abe, J. Nucl. Mater. 283 (2000) 1144–1147.
[14] M. Samaras, P.M. Derlet, H. Van Swygenhoven, M. Victoria, Phys. Rev. Lett. 88 (2002) 125505.
[15] X.M. Bai, A.F. Voter, R.G. Hoagland, M. Nastasi, B.P. Uberuaga, Science 327 (2010) 1631–1634.
[16] R. Liu, Y. Zhou, T. Hao, T. Zhang, X.P. Wang, C.S. Liu, Q.F. Fang, J. Nucl. Mater. 424 (2012) 171–175.
[17] Y. Kim, K.H. Lee, E.P. Kim, D.I. Cheong, S.H. Hong, Int. J. Refract. Met. Hard Mater 27 (2009) 842–846.
[18] M. Rieth, B. Dafferner, J. Nucl. Mater. 342 (2005) 20–25.
[19] M.A. Yar, S. Wahlberg, H. Bergqivist, H.G. Salem, M. Johnsson, M. Muhammed, J. Nucl. Mater. 412 (2011) 227–232.
[20] M.A. Yar, S. Wahlberg, H. Bergqvis, H.G. Salem, M. Johnsson, M. Muhammed, J. Nucl. Mater. 408 (2011) 129–135.
[21] A. Munoz, M.A. Monge, B. Savoini, M.E. Rabanal, G. Garces, R. Pareja, J. Nucl. Mater. 417 (2011) 508–511.
[22] I. Wesemann, W. Spielmann, P. Heel, A. Hoffmann, Int. J. Refract. Met. Hard Mater. 28 (2010) 687–691.
[23] G. Liu, G.J. Zhang, F. Jiang, X.D. Ding, Y.J. Sun, J. Sun, E. Ma, Nat. Mater. 12 (2013) 344–350.
[24] R. Liu, X.P. Wang, T. Hao, C.S. Liu, Q.F. Fang, J. Nucl. Mater. 450 (2014) 69–74.
[25] Z.M. Xie, R. Liu, Q.F. Fang, Y. Zhou, X.P. Wang, C.S. Liu, J. Nucl. Mater. 444 (2014) 175–180.
[26] R. Liu, Z.M. Xie, T. Hao, Y. Zhou, X.P. Wang, Q.F. Fang, C.S. Liu, J. Nucl. Mater. 451 (2014) 35–39.
[27] G. Sha, Y.B. Wang, X.Z. Liao, Z.C. Duan, S.P. Ringer, T.G. Langdon, Acta Mater. 57 (2009) 3123–3132.